Applied Physics Letters

The study of contact properties in edge-contacted graphene–aluminum Josephson junctions

Cite as: Appl. Phys. Lett. **121**, 243503 (2022); https://doi.org/10.1063/5.0135034
Submitted: 15 November 2022 • Accepted: 01 December 2022 • Published Online: 13 December 2022

Zhujun Huang, Neda Lotfizadeh, Bassel H. Elfeky, et al.

ARTICLES YOU MAY BE INTERESTED IN

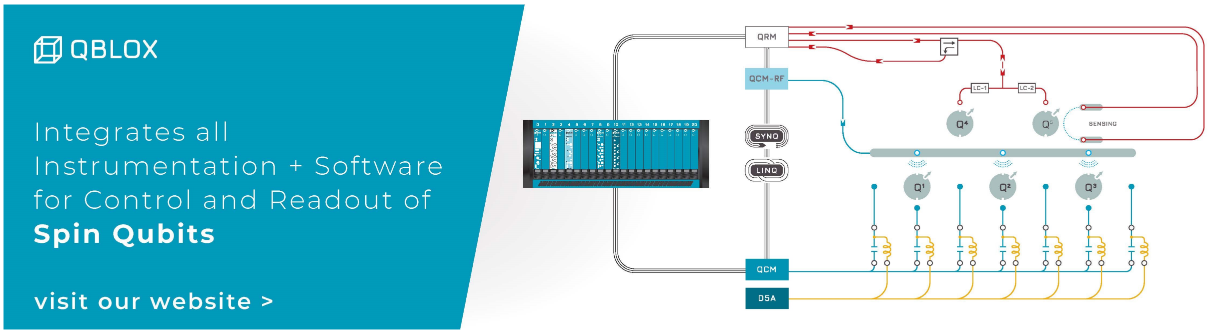

AIP Publishing

Applied Physics Letters ARTICLE scitation.org/journal/apl

The study of contact properties in edge-contacted graphene–aluminum Josephson junctions

Cite as: Appl. Phys. Lett. **121**, 243503 (2022); doi: 10.1063/5.0135034
Submitted: 15 November 2022 · Accepted: 1 December 2022 ·
Published Online: 13 December 2022

View Online Export Citation CrossMark

Zhujun Huang,[1] Neda Lotfizadeh,[2] Bassel H. Elfeky,[2] Kim Kisslinger,[3] Edoardo Cuniberto,[1] Peng Yu,[2] Mehdi Hatefipour,[2] Takashi Taniguchi,[4] Kenji Watanabe,[5] Javad Shabani,[2,a)] and Davood Shahrjerdi[1,6,a)]

AFFILIATIONS

[1]Electrical and Computer Engineering, New York University, Brooklyn, New York 11201, USA
[2]Department of Physics, New York University, New York, New York 10003, USA
[3]Center for Functional Nanomaterials, Brookhaven National Laboratory, Upton, New York 11973, USA
[4]International Center for Materials Nanoarchitectonics, National Institute of Materials Science, 1-1 Namiki Tsukuba, Ibaraki 305-0044, Japan
[5]Research Center for Functional Materials, National Institute of Materials Science, 1-1 Namiki Tsukuba, Ibaraki 305-0044, Japan
[6]Center for Quantum Phenomena, Department of Physics, New York University, New York, New York 10003, USA

[a)]Authors to whom correspondence should be addressed: jshabani@nyu.edu and davood@nyu.edu

ABSTRACT

Transparent contact interfaces in superconductor–graphene hybrid systems are critical for realizing superconducting quantum applications. Here, we examine the effect of the edge contact fabrication process on the transparency of the superconducting aluminum–graphene junction. We show significant improvement in the transparency of our superconductor–graphene junctions by promoting the chemical component of the edge contact etch process. Our results compare favorably with state-of-the-art graphene Josephson junctions. The findings of our study contribute to advancing the fabrication knowledge of edge-contacted superconductor–graphene junctions.

Graphene, due to its Dirac-like energy band structure, is a popular material for studying the interplay between superconductivity and quantum transport.[1–6] Two technical advances in fabricating graphene devices underlie this progress. The first is the ability to achieve ballistic transport in graphene through encapsulation in hexagonal boron nitride (hBN).[7] With this approach, the mean-free path (L_{mfp}) of hBN encapsulated graphene heterostructures (BGB) at cryogenic temperatures can exceed 20 μm.[7–9] The second advance is the adaptation of the edge contact process[7] for making superconducting contacts to BGB heterostructures.[10] The combination of these two features has enabled the studies of quantum Hall-based superconducting edge states[3–6] and numerous types of superconducting quantum circuits[11–15] in BGB Josephson junctions (JJ).

Recent studies have established the importance of the transparency at the superconductor–semiconductor interface for exploring proximity-induced superconductivity in the hybrid systems.[16–18] One figure-of-merit I_cR_n is often used to quantify the contact transparency in JJ devices,[19] where I_c is the critical supercurrent and R_n is the normal resistance of the junction. Theory predicts that graphene JJ with transparent contact should achieve $I_cR_n = 2.44\Delta/e$ in the short limit, where Δ is the superconducting gap.[20]

Previous demonstrations of edge-contacted graphene JJ devices reported significantly smaller I_cR_n/Δ than theory.[2,10,12–14,21] A possible reason for this observation is the short coherence length (ξ) of the superconductors (e.g., Nb, NbN, and MoRe) in those studies, which is comparable to or smaller than the graphene channel length (L_{ch}). This design constraint prevents the operation in the short limit, thereby making it difficult to assess the extent of graphene–superconductor transparency using I_cR_n/Δ.

A recent study reported a significant improvement in the normalized I_cR_n for edge-contacted graphene JJ devices, establishing the prospects of achieving operation in the short limit.[22] A key to this demonstration was the fabrication of short-channel ($L_{ch} < 0.2\ \mu$m) graphene devices that were contacted by an aluminum (Al) superconductor, which satisfies a requirement for short limit operation, i.e., $L_{ch} \ll \xi$ (coherence length of aluminum). More importantly, the high I_c (about 6 μA) of these short-channel graphene devices indicates high transparency at the superconductor–graphene interface. While edge-contacted graphene JJ has improved considerably, there is still significant room for enhancing their performance to reach the theoretical prediction. Studies of the structural, chemical, and electronic properties of the superconducting contacts to graphene are crucial for developing optimization strategies. Our work here is a step in this direction.

Here, we fabricated edge-contacted graphene devices with Al superconducting contacts as the test vehicle. Specifically, we examined the effect of the edge contact etch process on the performance of the resulting JJ devices. We observed that modifying this step can lead to significant enhancement in I_cR_n/Δ that outperforms JJ graphene devices with large Δ superconducting electrodes,[2,10,12–14,21] while matching the "second-to-champion" devices with Al superconducting electrodes.[22] Finally, we examined the structural properties and elemental composition of the contacts to graphene in our BGB JJ devices using high-resolution transmission electron microscopy (HRTEM). This analysis revealed the unintentional incorporation of carbon (C) and oxygen (O) impurities at the contact interface with graphene.

In this work, we used the poly(vinyl) alcohol (PVA)-assisted-graphene-exfoliation method to produce the monolayer graphene flakes.[23] A sub-10 nm PVA film was spin-coated onto Si substrates covered with SiO_2 and used as the adhesion promotion layer during the graphene exfoliation. The BGB heterostructures were constructed using the Quantum Material Press tool.[24] To achieve BGB heterostructures with atomically clean interfaces, we followed a stacking process, which allows the full removal of the polymeric contaminations across the entire dimensions of the heterostructures.[8] Before the fabrication of devices, we confirmed the monolayer graphene and the interface cleanliness using Raman spectroscopy[25] (see the supplementary material, Fig. S1).

Figure 1(a) shows the schematic illustration of a BGB JJ device, where graphene is edge-contacted by bilayer Ti/Al (10/30 nm) electrodes. In this structure, the silicon substrate functions as the global bottom gate. We observed that direct deposition of Al yields poor electrical contact to graphene. In contrast, we found experimentally that the incorporation of a 10-nm-thin Ti interlayer considerably improved the contact quality.

We employed a self-aligned process for fabricating the BGB JJ devices.[10] This fabrication process is useful for minimizing the polymer residues at the contact region, while relaxing the requirement of good alignment in the lithography step. We fabricated the graphene JJ devices by first defining a rectangle-shaped BGB mesa using a combination of e-beam lithography and an etching step. A subsequent lithography step defined the self-aligned metal contact regions, followed by reactive ion etch (RIE) of the BGB heterostructures that exposes the graphene edge for contacting to the metal electrodes. Finally, Ti/Al metal electrodes were formed through sputtering and liftoff processes.

We fabricated two sets of device samples (Al-1 and Al-2) by varying the edge contact etch process. Specifically, we employed two different CHF_3/O_2 gas mixtures by adjusting the flow rates (40/4 sccm for Al-1 and 60/4 sccm for Al-2 samples). Other etch conditions in this step were kept unchanged. Our rationale for this experimental design is that increasing this gas ratio is known to promote the chemical etching.[26] We hypothesized that promoting the chemical component of the BGB etch can be favorable for enhancing the chemical activation of the graphene edge to yield stronger coupling to the metal electrode.[27] Figure 1(b) shows the optical image of Al-1 JJ devices configured in a transfer-length-measurement (TLM) structure with $L_{ch} = 0.5$, 0.75, and 1 μm. We designed the JJ devices on Al-2 to include smaller L_{ch} than Al-1, with $L_{ch} = 0.3$, 0.4, and 0.6 μm. The channel widths of all devices are $W = 5\ \mu$m.

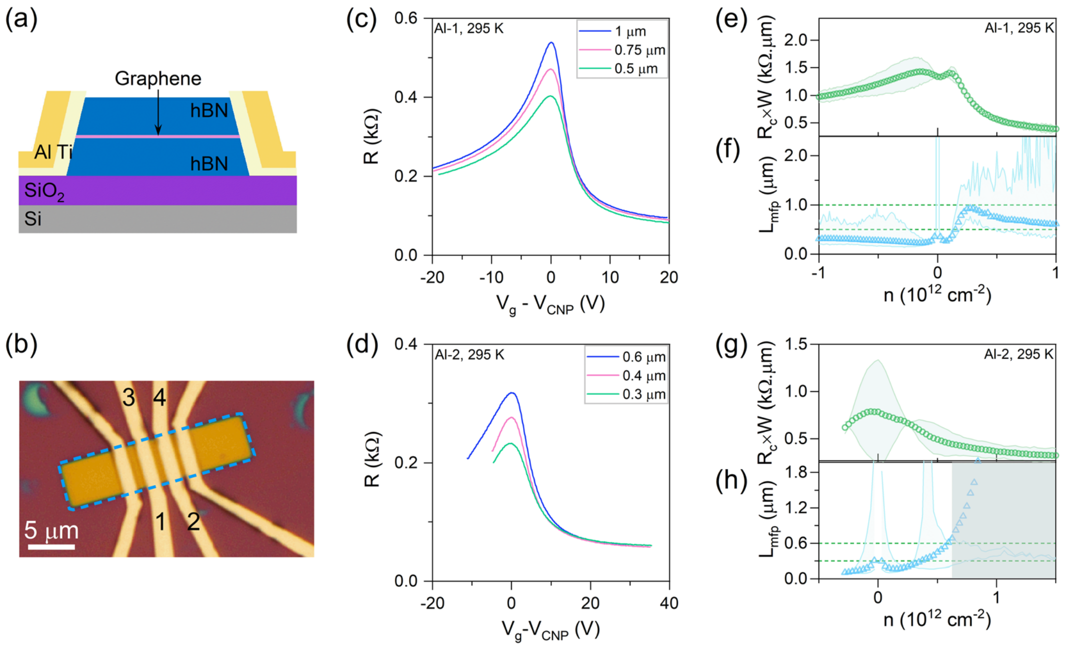

FIG. 1. Analysis of Al-graphene junction at room temperature. (a) Schematic illustration of the BGB JJ device contacted with Ti/Al. (b) Optical image of the BGB JJ devices from Al-1 sample. The BGB mesa is highlighted with a blue dashed box. Room temperature device resistance as a function of gate voltages in (c) Al-1 and (d) Al-2 devices. TLM analysis extracts (e) and (g) R_cW and (f) and (h) L_{mfp} from Al-1 and Al-2 devices, respectively.

Our electrical characterization of the BGB JJ devices initially focused on studying carrier transport in graphene at room temperature (Fig. 1) and low temperature of 1.5 K (Fig. 2). These measurements were performed using standard low-frequency lock-in technique with an excitation current of 5–10 nA. The BGB JJ devices had a quasi-four-point structure, which eliminates the resistance contribution from the metal electrode leads. The current was injected from lead 1 to 2, and the voltage was measured between leads 3 and 4 [see Fig. 1(b)]. This configuration measures the sum of the graphene channel resistance and contact resistance.

Figures 1(c) and 1(d) show the room temperature device resistance (R) as a function of the gate bias (V_g) for JJ devices on the Al-1 and Al-2 samples, respectively. In all devices, the total resistance exhibits an electron–hole asymmetry, where the hole branch has a higher resistance than the electron branch. This electron–hole asymmetry is attributed to the contact-induced electron doping.[2,10,28] This phenomenon yields the formation of p–n junctions at the contact region, creating an additional barrier for the hole carriers at the metal–graphene interfaces.

We employed TLM analysis to examine the contact resistance and carrier transport at room temperature. The width-normalized resistance can be written as a linear function of L_{ch} as follows:

$$RW = R_cW + R_{ch}W = R_cW + \frac{L_{ch}}{\sigma},$$

where R_c is the total contact resistance, R_{ch} is the graphene channel resistance, and σ is the graphene conductivity. By applying a linear fit to the TLM data (see the supplementary material, Fig. S2), we extracted the width-normalized R_c [see Figs. 1(e)–1(g)]. We also calculated the mean-free-path (L_{mfp}) by assuming diffusive transport in these devices. Figures 1(f)–1(h) show $L_{mfp} = \frac{h}{2e}\frac{\sigma}{k_F}$ as a function of carrier density, where k_F is the Fermi wavevector. This analysis revealed that Al-2 devices have a smaller R_c than Al-1 devices at high carrier density. Furthermore, we calculated $0.5\,\mu m < L_{mfp} < 1\,\mu m$ in Al-1 devices at high electron density, which is comparable to the device dimension [see Fig. 1(f)]. The resistance of the Al-2 devices at high electron density showed negligible channel-length dependence, which yielded $L_{mfp} \gg 0.6\,\mu m$ [marked by the gray shading in Fig. 1(h)]. The TLM analysis at room temperature suggests that the Al-1 and Al-2 devices operate in the crossover regime between the diffusive and ballistic transport.

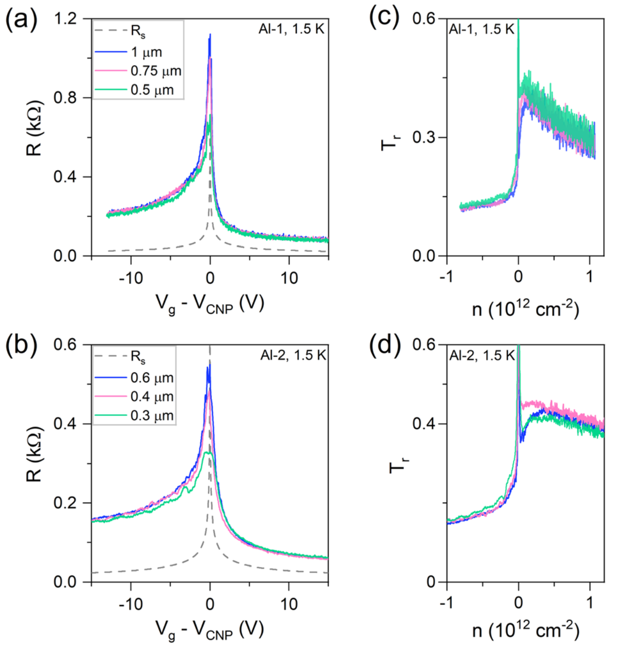

FIG. 2. Low temperature transport analysis. The graphene resistance as a function of gate voltage measured at 1.5 K for (a) Al-1 and (b) Al-2 devices. T_r calculated from Landauer's formula for (c) Al-1 and (d) Al-2 devices.

Next, we studied the low temperature transport at T = 1.5 K, which is above the superconducting critical temperature (T_c) of Al. Figures 2(a) and 2(b) show the gate voltage dependent plots of resistance for Al-1 and Al-2 devices, respectively. The data revealed negligible channel-length dependence of resistance away from the charge neutrality point (CNP), suggesting ballistic transport. Assuming ballistic transport in graphene, we investigated the metal–graphene contact properties. A ballistic conductor (i.e., $L_{mfp} > L_{ch}$) with no scattering centers has zero resistance. Therefore, the total resistance in a ballistic device can be attributed to the resistance in the immediate vicinity of the conductor–contact interfaces, which is known as the Sharvin resistance (R_s).[29–31] This quantum-limited resistance is determined by the number of conducting modes (M) in the ballistic conductor. Thus, the graphene Sharvin resistance can be written as

$$R_s^{-1} = G_s = g_0M = \frac{4e^2}{h}\,\mathrm{int}\left(\frac{k_FW}{\pi}\right),$$

where h is the Planck constant, g_0 is the conductance quantum, and the factor 4 comes from the spin and valley degeneracy in graphene. In Figs. 2(a) and 2(b), we plotted R_s to allow comparison with the measured device resistances. This analysis revealed an observable difference between the theoretical and measured values, suggesting that additional factors should be considered for describing the device resistance.

In Landauer's formula, a finite transmission probability (T_r) is used to account for the difference in R and R_s.[32] T_r describes the averaged probability of electron transmission from one metal contact to the other. Thus, the overall conductance G can be written as $G = G_sT_r$. From this equation, we extracted T_r as a function of the carrier density in graphene, as shown in Figs. 2(c) and 2(d). This analysis revealed that, at high electron density, Al-2 devices exhibit about 30% higher T_r than the Al-1 devices ($T_r \sim 0.4$ vs 0.3). While this analysis estimates the extent of the non-ideality in the ballistic transport of graphene devices, further studies are required to identify the exact sources of the finite T_r. For example, various non-idealities in the materials can contribute to the deviation of T_r from unity, such as disorders at the contact interfaces (i.e., graphene edge or metal electrode), non-specular boundary scattering in graphene, and mismatch of conducting modes between metal and graphene.[29,31] Nevertheless, this analysis revealed the noticeable role of the edge contact etch in our fabrication process in shaping the electronic properties of the contact.

Next, we evaluated the Josephson characteristics of the Al-1 and Al-2 devices. Figure 3 shows the representative Josephson dc measurements of the 0.4 μm device on the Al-2 device sample at 15 mK. The data show I_c of 1.63 and 0.3 μA at electron and hole carrier density of

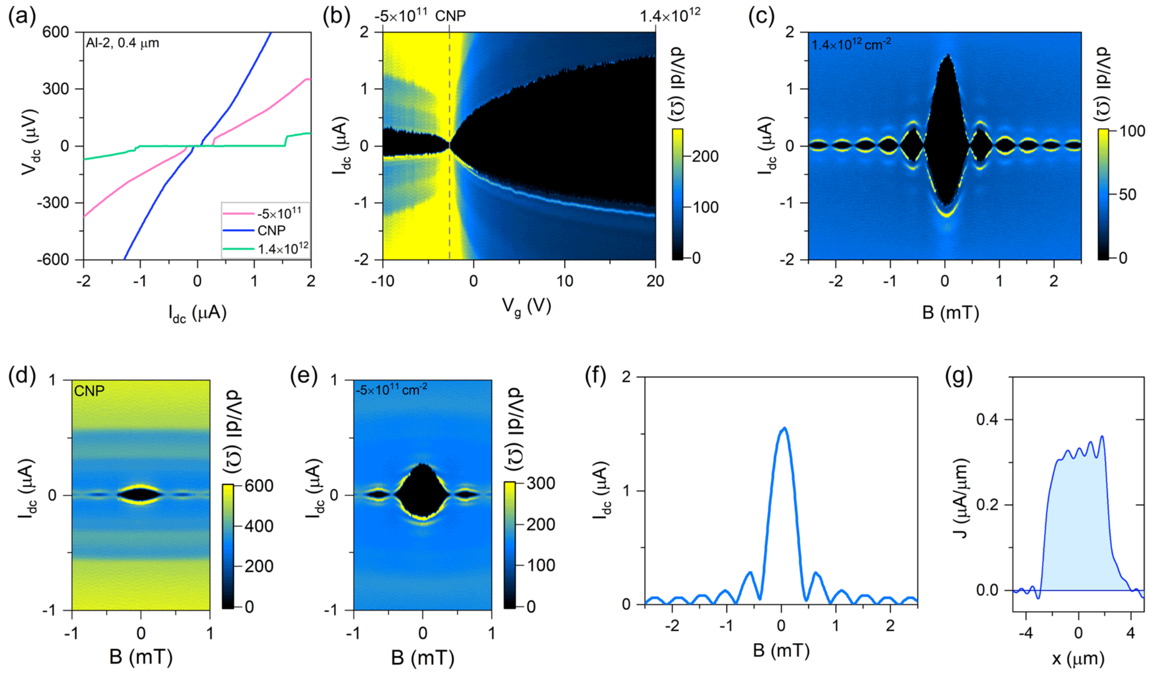

FIG. 3. Proximity-induced superconductivity in graphene. (a) V–I characteristics measured in the 0.4 μm device at different carrier concentrations at 15 mK. (b) Differential resistance as a function of bias current and gate voltage in the 0.4 μm BGB JJ device (carrier density legends are in units of cm^{-2}. "-" denotes hole carriers). Supercurrent shows Fraunhofer-like interference pattern on the (c) electron, (d) CNP, and (e) hole branch in the presence of a vertical magnetic field. (f) Critical current profile extracted from data in (c). Reconstructed current density distribution from data in (f).

1.4×10^{12} and -5×10^{11} cm^{-2}, respectively. These results confirm the gate tunability of the supercurrent. I_c increases with the carrier density on both electron and hole branches. Moreover, the minimum I_c (0.06 μA) occurs at the charge neutrality point (CNP). The differential resistance map in Fig. 3(b) revealed the electron–hole asymmetry in I_c. For the same carrier density, the electron branch provides over four times higher I_c than the hole branch. The considerably smaller I_c on the hole branch is due to the contact-induced doping.[2,10,28] These results confirm the proximity-induced superconductivity of graphene. We have provided the results of the other devices on Al-1 and Al-2 samples in the supplementary material, Fig. S3.

Next, we examined the supercurrent interference pattern in the presence of vertical magnetic field (B_z). These measurements provide information about the field profile in the junction by analyzing the node periodicity of the supercurrent.[33,34] Assuming a rectangular junction with uniform current distribution, the interference pattern follows:

$$I_c(B_z) = I_c^0 \left| \frac{\sin \pi\Phi/\Phi_0}{\pi\Phi/\Phi_0} \right|,$$

where Φ_0 is the flux quantum, Φ is the out-of-plane flux in the junction region, and I_c^0 is the zero-field critical current. In Figs. 3(c)–3(e), we plot the measured Fraunhofer patterns at different carrier density of 1.4×10^{12}, -5×10^{11} cm^{-2}, and CNP. The field oscillation frequency is 0.43 mT, which gives $L_{ch} + 2\lambda = 0.93\,\mu$m (hence $\lambda = 0.26\,\mu$m), where λ is the penetration depth into the Al electrodes.

Furthermore, we used these datasets to reconstruct the current density distribution of the junction.[35] Fig. 3(f) illustrates the critical current extracted from Fig. 3(c). In Fig. 3(g), we calculated current density profile, which shows nearly constant current density within the junction. This result implies a uniform contact quality and homogeneous transport properties in this BGB JJ device (see the supplementary material, Fig. S3, for measurements in other junctions).

The large I_c of 1.63 μA in Fig. 3(a) points to a good transparency at the Al–graphene junction. Therefore, we next examined the transparency of the superconducting Al–graphene junction by calculating I_cR_n. Figures 4(a) and 4(b) show the I–V curves of the Al-1 and Al-2 devices, measured at high electron density using a biasing current up to 10 μA. The use of high biasing current is an important consideration for accurate extraction of R_n as it must be extracted in the regime where the junction becomes fully Ohmic. From the slope of these I–V curves, we calculated $R_n \approx 90\,\Omega$ for Al-1 devices at 5×10^{11} cm^{-2}. For Al-2 devices, we obtained $R_n \approx 50\,\Omega$ at 1.4×10^{12} cm^{-2}. These extracted R_n values are consistent with the transport measurements at 1.5 K. Furthermore, we used the cold branch I–V curves in Figs. 4(a) and 4(b) to obtain I_c, providing $I_c = 0.6$, 0.46, and 0.38 μA for Al-1 devices and $I_c = 1.7$, 1.63, and 1.45 μA for Al-2 devices.

Figure 4(c) shows the summary of the I_cR_n data for Al-1 and Al-2 devices normalized to Δ of the superconductor (notice the star symbols in this plot). An important consideration in obtaining I_cR_n/Δ for evaluating the contact transparency is to use the bulk superconducting gap of Al.[17] To do so, we measured T_c of Al, which was 1.15 and 0.9 K in Al-1 and Al-2 samples, respectively. Correspondingly, the bulk superconducting gap of Al in Al-1 and Al-2 samples was 175 and 136 μeV, respectively. Using this information, we calculated I_cR_n/Δ to

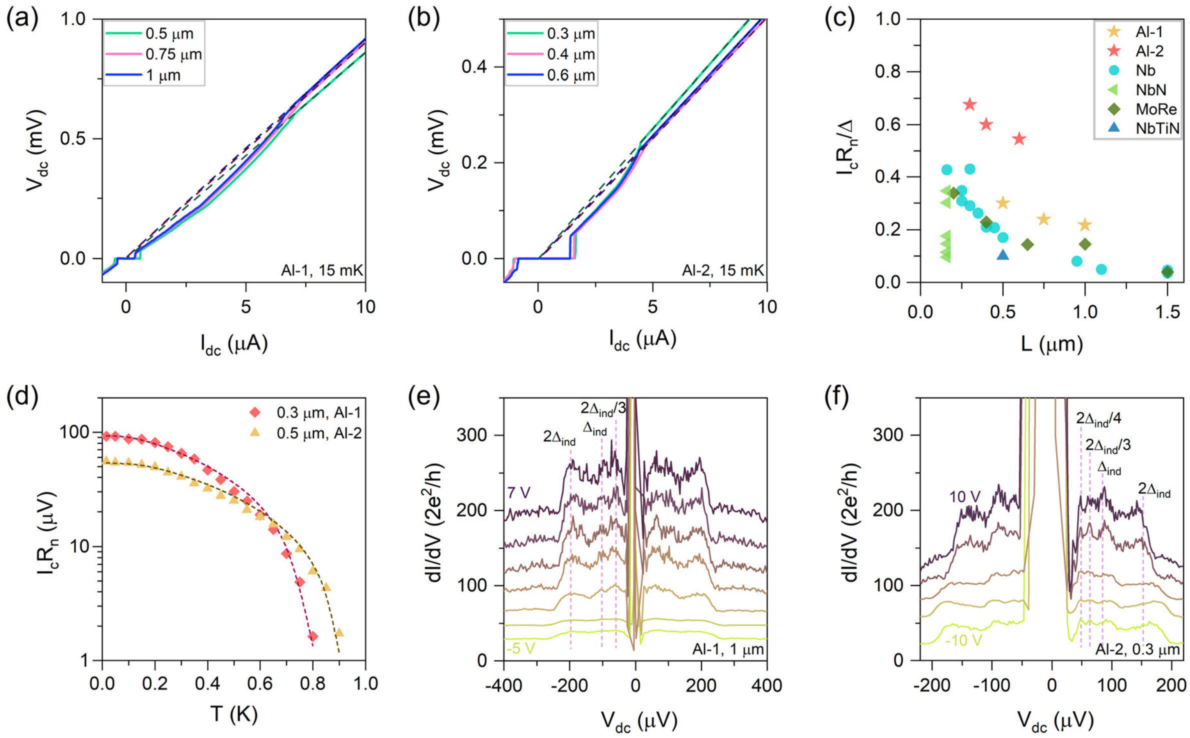

FIG. 4. Junction transparency of Al–graphene devices. (a) and (b) V–I characteristics of the Al-1 and Al-2 devices. (c) I_cR_n/Δ plotted as a function of device lengths, comparing our devices with other superconductor edge-contacted BGB devices. (d) Temperature dependent I_cR_n and the fitting for extracting α. MAR measures an induced gap of (e) $\Delta_{ind} = 100$ μeV in the Al-1 devices and (f) $\Delta_{ind} = 80$ μeV in the Al-2 devices. The dashed lines in MAR plots mark the conductance peak position of $2\Delta_{ind}/N$. The dI/dV curves are offset for better illustration.

be 0.3, 0.24, and 0.2 for Al-1 devices, and 0.68, 0.6, and 0.54 of Al-2 devices. Comparing I_cR_n/Δ of the devices with similar L_{ch} on Al-2 and Al-1 samples indicates almost two times improvement in the transparency of the superconducting Al–graphene junction. This analysis provides further evidence for the important role of the edge contact etch in our fabrication process.

To put these results in perspective, in Fig. 4(c), we compared I_cR_n/Δ of our devices with state-of-the-art counterparts that use large Δ superconductors.[2,10,12–14,21,36] For fair comparison in this plot, we normalized I_cR_n to the bulk superconducting gap for all data. This summary plot indicates higher I_cR_n/Δ of our devices relative to their counterparts with similar lengths. We attribute the observed improvement, in part, to the longer coherence length of Al in our devices.

The measurements of I_cR_n as a function of temperature can also provide information about the contact transparency.[19] Figure 4(d) shows the experimental I_cR_n for the 0.5 and 0.3 μm devices on Al-1 and Al-2 samples, respectively. From the data, we recovered $I_cR_n = \alpha\Delta/e$ using the Kulik–Omelyanchuk relation[37] and found $\alpha = 0.22$ and 0.43 for the 0.5 and 0.3 μm devices, respectively (see the supplementary material, Note 2). This analysis further confirms the improved junction transparency in the Al-2 devices.

Another important property of a JJ device is the induced superconducting gap Δ_{ind}, which can be obtained from the multiple Andreev reflection (MAR).[17] Figures 4(e) and 4(f) show the measured conductance of the 1 and 0.3 μm devices (on Al-1 and Al-2 samples) at different gate voltages. Several discernable conductance peaks can be observed in the conductance. The position of those peaks corresponds to the energy levels of $2\Delta_{ind}/N$, where N is an integer number. From Figs. 4(e) and 4(f), we extracted $\Delta_{ind} = 100$ and 80 μeV for Al-1 and Al-2 devices, respectively. Our observation of a smaller Δ_{ind} than the bulk superconducting gap is consistent with the previous studies on Al devices.[17] This analysis emphasizes the importance of normalizing I_cR_n to the bulk superconducting gap for assessing the junction transparency.

Finally, we analyzed the structural properties and elemental composition of the metal–graphene junction using HRTEM and electron dispersive x-ray spectroscopy (EDS). Figure 5(a) shows the cross-sectional HRTEM image of a BGB JJ with $L_{ch} = 0.5$ μm. Figure 5(b) shows the zoomed-in view of the same BGB JJ at the edge contact region. The HRTEM images confirmed the continuity of the Ti/Al metal stacks on the BGB sidewall. It also revealed the sharpness of the metal–BGB interface. The basal plane of the BGB layers is visible in Fig. 5(b), confirming the atomically clean interfaces between graphene and hBN layers. These results confirmed the excellent structural quality of the BGB stacks.

Figures 5(c)–5(g) show the individual EDS maps of different elements obtained from the same region as Fig. 5(b). These results together with the overlapped EDS image in Fig. 5(h), provided detailed information about the elemental composition of the metal–graphene junction. Figure 5(h) confirms the formation of the edge contact between graphene and the Ti layer. Curiously, this analysis also revealed the presence of elemental C and O atoms, which mainly

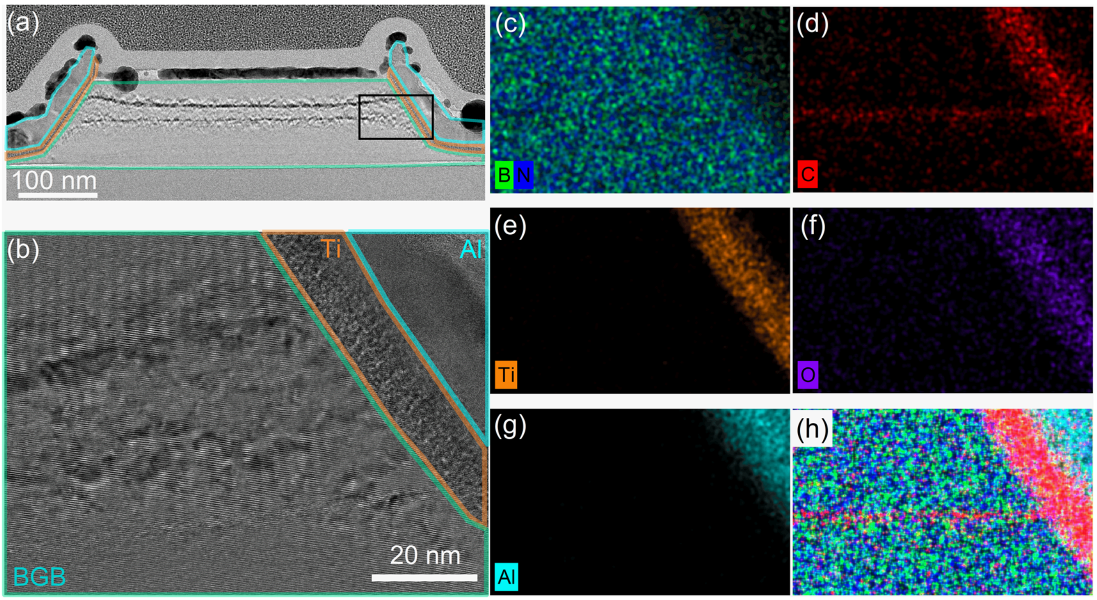

FIG. 5. HRTEM analysis of Al–graphene junction. (a) Cross-sectional HRTEM image of a BGB JJ with $L_{ch} = 0.5\,\mu$m. (b) Zoomed-in HRTEM image at the edge contact region, marked by a solid black box in (a). Elemental composition of the junction shows (c) boron and nitride, (d) C, (e) Ti, (f) O, and (g) Al elements. (h) Overlapping EDS map of all elements.

overlap with the Ti interlayer. In our experiment, we did not investigate the mechanism of O and C incorporation and the nature of their interactions with Ti. However, we suspect that the incorporation of these impurities occurs during the Ti deposition due to its known high reactivity with C and O.[38–40] While we do not know how these impurities affect the junction transparency, we conjecture that they may be a limiting factor in improving the performance of our graphene JJ devices. Therefore, a future research direction is to investigate the effect of alternative interlayers that are less susceptible to the unintentional incorporation of C and O impurities.

In conclusion, the results reported here illustrate the noticeable role of the edge contact etch in our fabrication process on the transparency of the superconducting Al–graphene junction. Specifically, we found that promoting the chemical component of the etch process was beneficial in improving the device performance. With this modification, the normalized I_cR_n of our devices surpassed that of state-of-the-art counterparts with large Δ (Refs. 2, 10, 12–14, 21, and 36) while matching the second-to-champion devices with Al (Ref. 22; see the supplementary material, Fig. S4). Furthermore, our HRTEM study revealed the presence of C and O impurities in the Ti interlayer. We conjecture that further improvement of junction transparency may require strategies for achieving an impurity–free metal interlayer. Finally, many studies have contributed to the persistent development of the edge contact fabrication process,[7,27,41] and this work adds an advance in this direction for improving the superconductor–graphene junction.

See the supplementary material for additional data for the electronic and materials characteristics of the graphene JJ devices.

D.S. acknowledges support from NSF CMMI (Award No. 2224139). J.S. acknowledges support from ARO (Grant Nos. W911NF-21-2-0169 and W911NF2210048). K.W. and T.T. acknowledge support from the Elemental Strategy Initiative conducted by the MEXT, Japan (Grant No. JPMXP0112101001) and JSPS KAKENHI (Grant Nos. 19H05790, 20H00354, and 21H05233). This work was performed in part at the ASRC NanoFabrication Facility of CUNY in New York. This research used resources of the Center for Functional Nanomaterials (CFN), which is a U.S. Department of Energy Office of Science User Facility, at Brookhaven National Laboratory under Contract No. DE-SC0012704. The authors acknowledge Dr. Suji Park of BNL for help with the operation of the QPress tool.

AUTHOR DECLARATIONS

Conflict of Interest

The authors have no conflicts to disclose.

Author Contributions

Zhujun Huang: Conceptualization (equal); Data curation (lead); Formal analysis (equal); Investigation (equal); Methodology (lead); Writing – original draft (equal); Writing – review & editing (equal). **Javad Shabani:** Conceptualization (equal); Formal analysis (equal); Writing – original draft (supporting); Writing – review & editing (supporting). **Davood Shahrjerdi:** Conceptualization (equal); Formal analysis (equal); Funding acquisition (lead); Investigation (equal); Writing – original draft (equal); Writing – review & editing (equal). **Neda Lotfizadeh:** Data curation (supporting); Formal analysis (supporting). **Bassel Heiba Elfeky:** Data curation (supporting); Formal analysis (supporting). **Kim Kisslinger:** Data curation (supporting); Formal analysis (supporting). **Edoardo Cuniberto:** Data curation (supporting); Methodology (supporting). **Peng Yu:** Data curation (supporting);

Methodology (supporting). **Mehdi Hatefipour:** Data curation (supporting). **Takashi Taniguchi:** Resources (supporting). **Kenji Watanabe:** Resources (supporting).

DATA AVAILABILITY

The data that support the findings of this study are available from the corresponding authors upon reasonable request.

REFERENCES

[1] F. Amet, C. T. Ke, I. V. Borzenets, J. Wang, K. Watanabe, T. Taniguchi, R. S. Deacon, M. Yamamoto, Y. Bomze, and S. Tarucha, Science **352**(6288), 966–969 (2016).
[2] M. B. Shalom, M. Zhu, V. Fal'Ko, A. Mishchenko, A. Kretinin, K. Novoselov, C. Woods, K. Watanabe, T. Taniguchi, and A. Geim, Nat. Phys. **12**(4), 318–322 (2016).
[3] G.-H. Lee, K.-F. Huang, D. K. Efetov, D. S. Wei, S. Hart, T. Taniguchi, K. Watanabe, A. Yacoby, and P. Kim, Nat. Phys. **13**(7), 693–698 (2017).
[4] Y. Ronen, T. Werkmeister, D. Haie Najafabadi, A. T. Pierce, L. E. Anderson, Y. J. Shin, S. Y. Lee, Y. H. Lee, B. Johnson, and K. Watanabe, Nat. Nanotechnol. **16**(5), 563–569 (2021).
[5] A. Seredinski, A. W. Draelos, E. G. Arnault, M.-T. Wei, H. Li, T. Fleming, K. Watanabe, T. Taniguchi, F. Amet, and G. Finkelstein, Sci. Adv. **5**(9), eaaw8693 (2019).
[6] L. Zhao, E. G. Arnault, A. Bondarev, A. Seredinski, T. F. Larson, A. W. Draelos, H. Li, K. Watanabe, T. Taniguchi, and F. Amet, Nat. Phys. **16**(8), 862–867 (2020).
[7] L. Wang, I. Meric, P. Huang, Q. Gao, Y. Gao, H. Tran, T. Taniguchi, K. Watanabe, L. Campos, and D. Muller, Science **342**(6158), 614–617 (2013).
[8] Z. Huang, E. Cuniberto, S. Park, K. Kisslinger, Q. Wu, T. Taniguchi, K. Watanabe, K. G. Yager, and D. Shahrjerdi, Small **18**(20), 2201248 (2022).
[9] D. Purdie, N. Pugno, T. Taniguchi, K. Watanabe, A. Ferrari, and A. Lombardo, Nat. Commun. **9**(1), 5387 (2018).
[10] V. E. Calado, S. Goswami, G. Nanda, M. Diez, A. R. Akhmerov, K. Watanabe, T. Taniguchi, T. M. Klapwijk, and L. M. Vandersypen, Nat. Nanotechnol. **10**(9), 761–764 (2015).
[11] I. Joel, J. Wang, D. Rodan-Legrain, L. Bretheau, D. L. Campbell, B. Kannan, D. Kim, M. Kjaergaard, P. Krantz, and G. O. Samach, Nat. Nanotechnol. **14**(2), 120–125 (2019).
[12] G.-H. Lee, D. K. Efetov, W. Jung, L. Ranzani, E. D. Walsh, T. A. Ohki, T. Taniguchi, K. Watanabe, P. Kim, and D. Englund, Nature **586**(7827), 42–46 (2020).
[13] E. D. Walsh, W. Jung, G.-H. Lee, D. K. Efetov, B.-I. Wu, K.-F. Huang, T. A. Ohki, T. Taniguchi, K. Watanabe, and P. Kim, Science **372**(6540), 409–412 (2021).
[14] F. E. Schmidt, M. D. Jenkins, K. Watanabe, T. Taniguchi, and G. A. Steele, Nat. Commun. **9**(1), 4069 (2018).
[15] J. Kroll, W. Uilhoorn, K. van der Enden, D. de Jong, K. Watanabe, T. Taniguchi, S. Goswami, M. Cassidy, and L. P. Kouwenhoven, Nat. Commun. **9**(1), 4615 (2018).
[16] W. Chang, S. Albrecht, T. Jespersen, F. Kuemmeth, P. Krogstrup, J. Nygård, and C. M. Marcus, Nat. Nanotechnol. **10**(3), 232–236 (2015).
[17] M. Kjærgaard, H. J. Suominen, M. Nowak, A. Akhmerov, J. Shabani, C. Palmstrøm, F. Nichele, and C. M. Marcus, Phys. Rev. Appl. **7**(3), 034029 (2017).
[18] J. Shabani, M. Kjærgaard, H. J. Suominen, Y. Kim, F. Nichele, K. Pakrouski, T. Stankevic, R. M. Lutchyn, P. Krogstrup, and R. Feidenhans, Phys. Rev. B **93**(15), 155402 (2016).
[19] W. Mayer, J. Yuan, K. S. Wickramasinghe, T. Nguyen, M. C. Dartiailh, and J. Shabani, Appl. Phys. Lett. **114**(10), 103104 (2019).
[20] M. Titov and C. W. Beenakker, Phys. Rev. B **74**(4), 041401 (2006).
[21] I. Borzenets, F. Amet, C. Ke, A. Draelos, M. Wei, A. Seredinski, K. Watanabe, T. Taniguchi, Y. Bomze, and M. Yamamoto, Phys. Rev. Lett. **117**(23), 237002 (2016).
[22] J. Park, J. H. Lee, G.-H. Lee, Y. Takane, K.-I. Imura, T. Taniguchi, K. Watanabe, and H.-J. Lee, Phys. Rev. Lett. **120**(7), 077701 (2018).
[23] Z. Huang, A. Alharbi, W. Mayer, E. Cuniberto, T. Taniguchi, K. Watanabe, J. Shabani, and D. Shahrjerdi, Nat. Commun. **11**, 3029 (2020).
[24] See https://www.bnl.gov/qpress/ for "Qpress."
[25] C. Neumann, S. Reichardt, P. Venezuela, M. Drögeler, L. Banszerus, M. Schmitz, K. Watanabe, T. Taniguchi, F. Mauri, and B. Beschoten, Nat. Commun. **6**(1), 8429 (2015).
[26] R. Legtenberg, H. Jansen, M. D. Boer, and M. Elwenspoek, J. Electrochem. Soc. **142**(6), 2020 (1995).
[27] J. Son, J. Kwon, S. Kim, Y. Lv, J. Yu, J.-Y. Lee, H. Ryu, K. Watanabe, T. Taniguchi, and R. Garrido-Menacho, Nat. Commun. **9**(1), 3988 (2018).
[28] M. T. Allen, O. Shtanko, I. C. Fulga, J. I.-J. Wang, D. Nurgaliev, K. Watanabe, T. Taniguchi, A. R. Akhmerov, P. Jarillo-Herrero, and L. S. Levitov, Nano Lett. **17**(12), 7380–7386 (2017).
[29] M. De Jong, Phys. Rev. B **49**(11), 7778 (1994).
[30] S. Tarucha, T. Saku, Y. Tokura, and Y. Hirayama, Phys. Rev. B **47**(7), 4064 (1993).
[31] Y. V. Sharvin, Sov. Phys. JETP **21**, 655 (1965).
[32] S. Datta, *Electronic Transport in Mesoscopic Systems* (Cambridge University Press, 1997).
[33] R. Dynes and T. Fulton, Phys. Rev. B **3**(9), 3015 (1971).
[34] H. Suominen, J. Danon, M. Kjaergaard, K. Flensberg, J. Shabani, C. Palmstrøm, F. Nichele, and C. Marcus, Phys. Rev. B **95**(3), 035307 (2017).
[35] B. H. Elfeky, N. Lotfizadeh, W. F. Schiela, W. M. Strickland, M. Dartiailh, K. Sardashti, M. Hatefipour, P. Yu, N. Pankratova, and H. Lee, Nano Lett. **21**(19), 8274–8280 (2021).
[36] G. Nanda, J. L. Aguilera-Servin, P. Rakyta, A. Kormányos, R. Kleiner, D. Koelle, K. Watanabe, T. Taniguchi, L. M. Vandersypen, and S. Goswami, Nano Lett. **17**(6), 3396–3401 (2017).
[37] K. Delin and A. Kleinsasser, Supercond. Sci. Technol. **9**(4), 227 (1996).
[38] K. M. Freedy, T. E. Beechem, P. M. Litwin, M. G. Sales, M. Huang, R. S. Ruoff, and S. J. McDonnell, ACS Appl. Nano Mater. **1**(9), 4828–4835 (2018).
[39] C. Gong, S. McDonnell, X. Qin, A. Azcatl, H. Dong, Y. J. Chabal, K. Cho, and R. M. Wallace, ACS Nano **8**(1), 642–649 (2014).
[40] M. Popinciuc, V. E. Calado, X. L. Liu, A. R. Akhmerov, T. M. Klapwijk, and L. M. Vandersypen, Phys. Rev. B **85**(20), 205404 (2012).
[41] Q. Gao and J. Guo, APL Mater. **2**(5), 056105 (2014).